

Physical-point Lattice QCD study of baryon-baryon interactions in the $S = -1$ channel

Koichi Murase,^{a,*} Takumi Doi^b and Takahiro M. Doi^c

On behalf of the HAL QCD Collaboration

^aResearch Center for Nuclear Physics, The University of Osaka, Ibaraki, Osaka 567-0047, Japan

^bRIKEN Center for Interdisciplinary Theoretical and Mathematical Sciences Program (iTHEMS), RIKEN, Wako 351-0198, Japan

^cDepartment of Physics, Faculty of Science, Kyoto University, Kyoto 606-8502, Japan

E-mail: kmurase@rcnp.osaka-u.ac.jp

We study the baryon–baryon interactions in the strangeness $S = -1$ sector by applying the time-dependent HAL QCD method to the $N_f = 2 + 1$ gauge configurations generated at the physical point $(m_\pi, m_K) = (137, 502)$ MeV (HAL-conf-2023). We analyze the S -wave $N\Lambda$ – $N\Sigma$ coupled channels ($I = 1/2$, 1S_0 and 3S_1) and $N\Sigma$ ($I = 3/2$, 1S_0 and 3S_1) channels. The extracted potentials for $N\Sigma(I = 1/2, ^1S_0)$ and $N\Sigma(I = 3/2, ^3S_1)$ severely suffer from inelastic excited-state contamination at small times and large statistical fluctuations at larger times. We focus on $N\Sigma(I = 3/2, ^3S_1)$ and try to remove the inelastic contamination by extrapolation to $t \rightarrow \infty$ under a simple assumption on the time dependence of the potential. We examine the time dependence of the phase shifts and compare them with data from the J-PARC E40 experiment. We find that the extrapolation method seems to work very well in removing the inelastic contamination.

*The 42nd International Symposium on Lattice Field Theory (LATTICE2025)
2-8 November 2025
Tata Institute of Fundamental Research, Mumbai, India*

*Speaker

1. Introduction

Baryon–baryon interactions involving strangeness provide a natural extension of ordinary nuclear forces and offer a unique opportunity to explore the role of hadronic interactions beyond the nucleon sector. Among them, the strangeness $S = -1$ sector represents the minimal and most accessible extension, where hyperons appear as additional degrees of freedom while keeping close connections to conventional nuclear physics. Because of this minimal strangeness content, the $S = -1$ interactions are expected to play a phenomenologically important role in a wide range of physical systems.

The dense baryonic matter in neutron stars is an important example in nature. The onset of hyperons in dense matter modifies the equation of state through hyperon–nucleon and hyperon–nucleon–nucleon interactions, which leads to a softening of the pressure and affecting the mass–radius relation of neutron stars. The tension between this softening and the observation of massive neutron stars [1, 2], known as the hyperon puzzle, highlights the necessity of a quantitative and reliable description of the $S = -1$ interactions. The same interactions also manifest themselves in the properties of an independent nucleus. Hypernuclear spectroscopy provides constraints on the effective hyperon–nucleon interaction through the binding energies of Λ hypernuclei [3, 4], which reflect both two-body and three-body components of the $S = -1$ sector. These observables offer constraints complementary to those obtained from dense matter. Direct information on the $S = -1$ interactions can be obtained from scattering experiments [5, 6]. Although the available data are limited compared to the nucleon–nucleon case, hyperon–nucleon scattering remains the most feasible experimental approach in the strange sector. Observables such as total and differential cross sections, phase shifts, and cusp structures [7] associated with channel coupling encode the information on the coupled-channel dynamics, e.g. in the $N\Lambda$ – $N\Sigma$ system for the $S = -1$ sector. Hyperon interactions also play an important role in high-energy nuclear collision experiments, where a large number of strange hadrons are produced. Collective dynamics of hyperons are largely affected by the interaction in the $S = -1$ channel with the surrounding nucleons [8], which are observed as identified flow observables in high-energy nuclear collisions. Furthermore, femtoscopic two-particle correlations measured in high-energy nuclear collisions have recently emerged as a powerful and novel approach to probe hadron–hadron interactions. The momentum correlations of hadron pairs emitted from the fireball created in the collision reactions are sensitive to the relative wave function distorted by the interactions between the pair, which can be utilized to constrain the hadron–hadron interactions [9]. In this direction, the correlation functions between various hadrons are intensively measured in high-multiplicity p+p collisions [11] and nuclear collisions [10].

In this context, it is important to provide reliable and quantitative references for the $S = -1$ interactions based on state-of-the-art lattice QCD calculations, which can be compared to experimental observables or can be used as inputs to the effective models. We here focus on the baryon–baryon potentials in the $S = -1$ sector, which involves ground state baryons N , Λ , and Σ . We apply the time-dependent HAL QCD method [12, 13] to the latest lattice gauge configurations (HAL-conf-2023) [14] with $N_f = 2 + 1$ flavors on the physical-point masses of $m_\pi = 137.1(0.3)_{(-0.2)}^{(+0.0)}$ MeV and $m_K = 501.8(0.3)_{(-0.7)}^{(+0.0)}$ MeV.

A major challenge in the $S = -1$ comes from the fact that it has the worst signal-to-noise ratio compared to the other strange systems ($S \leq -2$) for the baryon–baryon interactions. This forces us

to look at a smaller Euclidean time t/a to obtain meaningful values for the potential, where inelastic excited states may not be sufficiently suppressed, depending on the channel, and thus contaminate the resulting potentials. In this study, we attempt to improve this situation by making use of global information in a wider range of the Euclidean time t/a , rather than relying on a local set of time slices through the simple application of the time-dependent HAL QCD method. We here report the current status of such an attempt based on a simple assumption that the inelastic contaminations enter in the potential in the sum of exponential forms.

2. HAL QCD Method

We consider coupled-channel analyses of the $N\Lambda-N\Sigma$ system with isospin $I = 1/2$, and single-channel analyses of the $N\Sigma$ system with isospin $I = 3/2$. To investigate the inelastic contamination (as will be discussed in Sec. 3), we consider only the S wave part in the present study; we consider two spin channels, 1S_0 and 3S_1 , for both $I = 1/2$ and $I = 3/2$. It should be noted that it is physically important to consider the tensor forces and the D wave in the future. We use the time-dependent HAL QCD method [13] to extract the potential $U(\vec{r}, \vec{r}')$ from the normalized four-point correlator $R^c_d(t, r)$ using the time-dependent Schrödinger equation with channel coupling:

$$\left(\frac{1 + 3\delta_c^2}{8\mu_c} \frac{\partial^2}{\partial t^2} - \frac{\partial}{\partial t} + \frac{\nabla^2}{2\mu_c} \right) R^c_d(\vec{r}, t) = \sum_{c'} \int d^3r' U^c_{c'}(\vec{r}, \vec{r}') \Delta^c_{c'} R^{c'}_d(\vec{r}', t), \quad (1)$$

where the subscripts c , c' , and d are labels of the channels, including the particle species ($N\Lambda$ or $N\Sigma$) and spin indices. The constant μ_c denotes the reduced mass of channel c , and $\delta_c = (m_{c_1} - m_{c_2}) / (m_{c_1} + m_{c_2})$ where m_{c_1} and m_{c_2} are the masses of two baryons in channel c . The factor $\Delta^c_{c'} = \exp[-(m_{c'_1} + m_{c'_2})t] / \exp[-(m_{c_1} + m_{c_2})t]$ is a correction for the mass difference between the channels. The R correlator is measured on gauge configurations as

$$R^c_d(\vec{r}, t) = \frac{\sum_{\vec{x}} \langle 0 | B_{c_1}(\vec{x} + \vec{r}, t) B_{c_2}(\vec{x}, t) \bar{J}_d | 0 \rangle}{\sqrt{Z_{c_1} Z_{c_2}} \exp[-(m_{c_1} + m_{c_2})t]}, \quad (2)$$

where B_{c_1} and B_{c_2} denote the interpolating operators of baryons c_1 and c_2 contained in channel c , and \bar{J}_d denotes the wall source for channel d . The isospin and spin projection for $I = 1/2$ or $3/2$ and 1S_0 or 3S_1 may additionally be performed. The wave-function renormalization factor $\sqrt{Z_j}$ represents the overlap of B_j with the ground-state baryon and can be determined by $\sqrt{Z_j} = A_j^{\text{PS}} \sqrt{2m_j / A_j^{\text{SS}}}$, where A_j^{PS} and A_j^{SS} are the coefficients of the two-point functions fitted by the forms,

$$C_j^{\text{PS}}(t) \approx A_j^{\text{PS}} \exp(-m_j t), \quad C_j^{\text{SS}}(t) \approx A_j^{\text{SS}} \exp(-m_j t). \quad (3)$$

Here, $C_j^{\text{PS}}(t)$ and $C_j^{\text{SS}}(t)$ are the two-point functions for baryon j with the point and wall sinks, respectively, with the wall source. In the actual calculations, the denominator of Eq. (2) is evaluated by the two-point functions as

$$\sqrt{Z_{c_1} Z_{c_2}} \exp[-(m_{c_1} + m_{c_2})t] \approx \sqrt{\frac{2m_{c_1}}{A_{c_1}^{\text{SS}}}} C_{c_1}^{\text{PS}}(t) \sqrt{\frac{2m_{c_2}}{A_{c_2}^{\text{SS}}}} C_{c_2}^{\text{PS}}(t), \quad (4)$$

which is effective in canceling a part of the statistical fluctuations in the numerator. To determine the potential, we assume a local potential of the form $U^c_d(\vec{r}, \vec{r}') = V^c_d(\vec{r})\delta(\vec{r} - \vec{r}')$, which is the leading order of derivative expansion of the non-local potential $U(\vec{r}, \vec{r}')$ with respect to $\vec{r}' - \vec{r}$ for the S wave. In this setup, the potential $V^c_d(\vec{r})$ can be straightforwardly obtained by the matrix inversion of $R^c_d(\vec{r}, t)$.

For the gauge configurations, previous studies [15, 16] used the so-called K-conf, which contains about 400 configurations generated on the K computer for $N_f = 2 + 1$ flavors mostly at the physical-point masses, $(m_\pi, m_K) = (146, 525)$ MeV. In this study, we use the so-called F-conf (HAL-conf-2023) [14] consisting of 1600 configurations generated on the Fugaku supercomputer for $N_f = 2 + 1$ flavors at the physical point $(m_\pi, m_K) = (137, 502)$ MeV in the volume $(96a)^4$ with lattice spacing $a = 0.084372(54)$ fm. The baryon masses in the lattice unit are determined to be $am_N = 0.4018(3)$, $am_\Lambda = 0.4785(10)$, and $am_\Sigma = 0.5139(11)$.

In this study, to extract the S -wave component of the R correlator, we first perform the projection of $R(\vec{r}, t)$ onto the trivial representation A_1^+ of the cubic group O_h :

$$\mathcal{P}^{(A_1^+)}[R(\vec{r}, t)] := \frac{1}{48} \sum_{g \in O_h} c^{(A_1^+)}(g) R(g^{-1}\vec{r}, t), \quad (5)$$

where $c^{(A_1^+)}(g) \equiv 1$. We then apply the Misner method [17] in the image of the A_1^+ projection. The basis of the Misner method significantly reduces in the A_1^+ image, because the spherical harmonics $Y_l^m(\theta, \phi)$ mostly vanish, i.e., $\mathcal{P}^{(A_1^+)}[Y_l^m] = 0$ if $l = 2$, $l \not\equiv 0 \pmod{2}$, or $m \not\equiv 0 \pmod{4}$, and because some are degenerate, e.g., $\mathcal{P}^{(A_1^+)}[Y_l^{4m}] = \mathcal{P}^{(A_1^+)}[Y_l^0]$ ($l = 4, 6, 8$, and 10). Therefore, including angular momentum up to $l = 6$, the angular part of the basis consists of only three linearly independent components,

$$\mathcal{P}^{(A_1^+)}[Y_l^0], \quad l = 0, 4, 6. \quad (6)$$

For the radial part, to obtain the potential at distance r , we use the Legendre polynomials centered at r up to the order $n = 3$,

$$P_n(\max\{-1, \min\{1, (r' - r)/\Delta\}\}), \quad n = 0, 1, 2, 3, \quad (7)$$

with the width $\Delta/a = 1$. We evaluate the R correlator and its radial derivatives at $r' = r$. In Eq (7), we restricted the argument of the Legendre polynomials within the interval $[-1, 1]$ to reduce spurious oscillations, which become prominent in noisy channels that we currently focus on. It is noted that the weights of the lattice points used in the Misner method [17] has support slightly outside the range $[r - \Delta, r + \Delta]$. In this study, we extract the r -dependence of the $l = 0$ component for the S wave. The time derivatives in Eq. (1) are evaluated by the finite central differences using the three consecutive time slices. The resulting potential is labeled by the Euclidean time t/a of the middle time slice.

3. Potentials and inelastic contamination

Figure 1 shows the full set of the potentials in the $S = -1$ sector obtained by the Misner method: the coupled-channel $N\Lambda$ - $N\Sigma$ potentials for the $I = 1/2$ channel and the single-channel

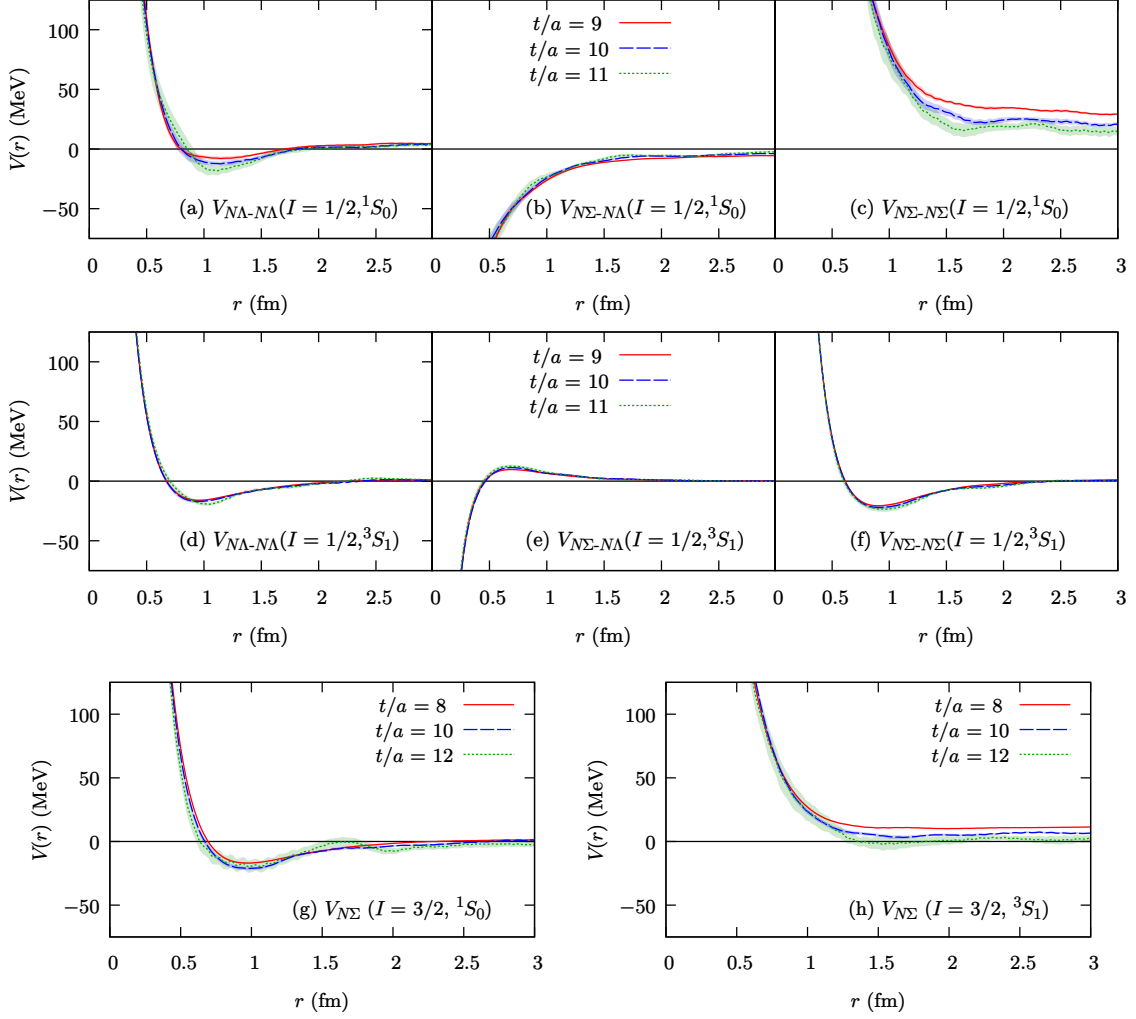


Figure 1: Potentials for 1S_0 and 3S_1 in both the $I = 1/2$ and $I = 3/2$ sectors. For the $I = 1/2$ sector with the $N\Lambda$ - $N\Sigma$ coupled-channel analysis, panels (a)–(c) show 1S_0 the potentials of 3S_1 , and panels (d)–(f) the potentials of 3S_1 . For the $I = 3/2$ sector in the single channel $N\Sigma$, panels (g) and (h) show the potentials for 1S_0 and 3S_1 , respectively. Different lines correspond to the potentials extracted at different time slices t/a . The band with higher colors show the statistical errors.

$N\Sigma$ potentials for the $I = 3/2$ channel, each containing both the S -wave spin-singlet (1S_0) and triplet (3S_1) channels. The coupled-channel potentials ($I = 1/2$) are represented in the 2×2 hermitian matrices, whose components are shown in Fig. 1 with the basis being $N\Lambda$ and $N\Sigma$. The ($I = 1/2, ^1S_0$) channel shown in panels (a)–(c) corresponds to the irreducible representations $\mathbf{27}$ and $\mathbf{8}_s$ of flavor $SU(3)$. Similarly, the ($I = 1/2, ^3S_1$) channel in panels (d)–(f) corresponds to the representations $\mathbf{10}$ and $\mathbf{8}_a$, the ($I = 3/2, ^1S_0$) channel in panel (g) to $\mathbf{27}$, and the ($I = 3/2, ^3S_1$) channel in panel (h) to $\mathbf{10}$.

Here, we shall focus on $V_{N\Sigma-N\Sigma}(I = 1/2, ^1S_0)$ in Fig. 1(c) and $V_{N\Sigma}(I = 3/2, ^3S_1)$ in Fig. 1(h), corresponding to the representations $\mathbf{8}_s$ and $\mathbf{10}$, respectively, which are fully or partially forbidden by the Pauli principle at the quark level. The potentials in those Pauli-forbidden channels are purely

repulsive without an attractive pocket. They have an issue of a constant offset of the potential at large r : Although the strong force should exponentially be suppressed at large r in the scale of the pion mass, those repulsive potentials do not vanish at large r and typically converges to a finite value at large r . The non-zero constant offset is particularly significant at a smaller Euclidean time t/a . This spurious behavior comes from contamination of inelastic excited states into the four-point function measured on the lattice. Since the interpolating operators in the source and sink do not only probe the target ground states but overlap with various inelastic excited states of the same quantum numbers, in general, the four-point functions contain contributions from all those states:

$$R(r, t) = \sum_i A_i \psi_{\text{el},i}(r) e^{-\Delta E_{\text{el},i} t} + \sum_i B_i \psi_{\text{inel},i}(r) e^{-\Delta E_{\text{inel},i} t}, \quad (8)$$

where $\psi_{\text{el},i}(r)$ and $\psi_{\text{inel},i}(r)$ represent the wave functions of the elastic and inelastic states at their energy levels $\Delta E_{\text{el},i}$ and $\Delta E_{\text{inel},i}$ relative to the ground-state energy. The elastic contributions in the first summation in Eq. (8) follow the Schrödinger equation (1), but it is not the case for the inelastic contributions in the second summation in Eq. (8), which results in unphysical constant shifts in the obtained potentials. One can naively understand the constant positive offset at large r as the contribution of the mass difference between the excited inelastic states and the target baryon system, which is independent of the distance r .

The inelastic contamination can usually be suppressed by looking at sufficiently large t/a , where the inelastic contributions are relatively more suppressed because of the larger energy $\Delta E_{\text{inel},i}$. However, if one considers too large t/a , the signal of the elastic contributions is also suppressed by the ground-state energy, and the statistical error becomes dominant finally. To obtain meaningful results of the potentials, one needs to find a time window where the time is not too small to be affected by inelastic contamination, and the time is not too large to be overwhelmed by the statistical fluctuations. In the Pauli-forbidden channels $V_{N\Sigma-N\Sigma}(I = 1/2, {}^1S_0)$ and $V_{N\Sigma}(I = 3/2, {}^3S_1^S)$, it becomes hard to find the available window because of smaller overlap of the operators with the target state. This is the current major issue for obtaining conclusive HAL QCD potentials for the $S = -1$ sector.

4. Extrapolation in time

The issue with inelastic contamination should ultimately be resolved systematically by, e.g., considering improved source/sink operators or solving general eigenvalue problems with various sources/sinks. However, we here try to determine the potential using the currently available four-point functions maximally. The conventional time-dependent HAL QCD method calculates the potentials $V(r)$ using the normalized four-point function $R(\mathbf{r}, t)$ from local t/a slices as described in Sec. 2, but we may try to utilize the global information of $R(\mathbf{r}, t)$ in t/a to determine the potential.

In this study, we focus on the potential of $N\Sigma(I = 3/2)$. We first calculate the time dependence of the potential $V(r, t)$ using the conventional HAL QCD method in Sec. 2, and try to remove the inelastic contamination by extrapolating the potential $V(r, t)$ to $t \rightarrow \infty$ by assuming a simple form

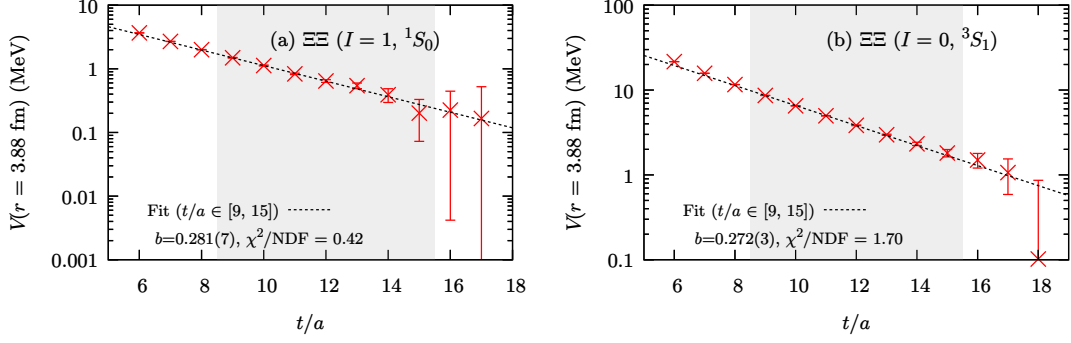


Figure 2: Time dependence of the S -wave potentials of $\Xi\Xi$ at $r = 3.88$ fm. The potential values are plotted in the logarithmic scale. The dotted line shows the result of the exponential fitting. The shaded area shows the fitting range. The fitted values of b and chi-square values are shown in the plot. The exponent is shown in the lattice unit. The chi square is calculated in the uncorrelated form, which ignores the correlations between different time points.

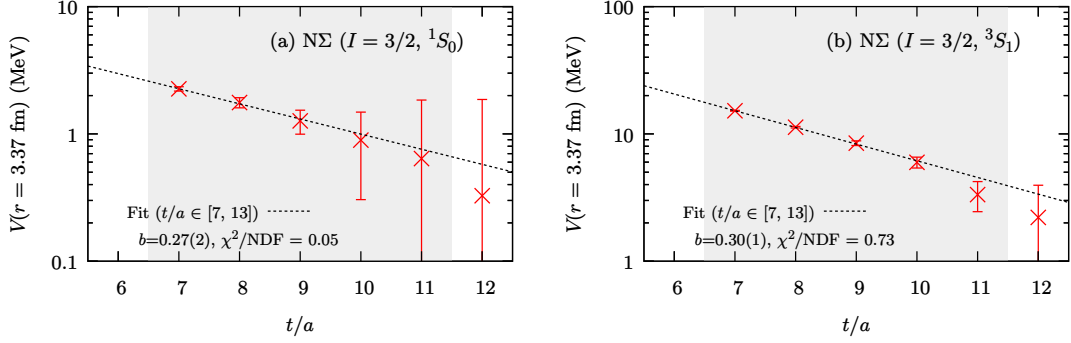


Figure 3: Time dependence of the S -wave potentials of $N\Sigma$ at $r = 3.37$ fm, obtained in the same way as Fig. 3.

of the time dependence of the potential:

$$\begin{aligned}
 V(r, t) &= V_{\text{el}}(r) + \sum_c V_{\text{inel},c}(r) e^{-b_c t} \\
 &\simeq V_{\text{el}}(r) + V_{\text{inel}}(r) e^{-bt} .
 \end{aligned} \tag{9}$$

In general, the potential will receive the contamination in the form of the first line in Eq. (9). The first term is the potential we want to extract and comes from the elastic contributions in the first term of Eq. (8), while the second term coming from inelastic contributions of Eq. (8) is written in the sum of different inelastic channels. In the present analysis for $N\Sigma(I = 3/2)$, as in the second line of Eq. (9), we only consider the most dominant inelastic contribution in the potential because we do not have a sufficient number of time points. The validity of this assumption can be tested with the channels with smaller noises, where a wide range of time points is available. Figure 2 shows the time dependence of the potentials of $\Xi\Xi$ at $r = 3.88$ fm in the logarithmic scale. The points turn out to be mostly aligned on a straight line. The dotted line shows the result of the single

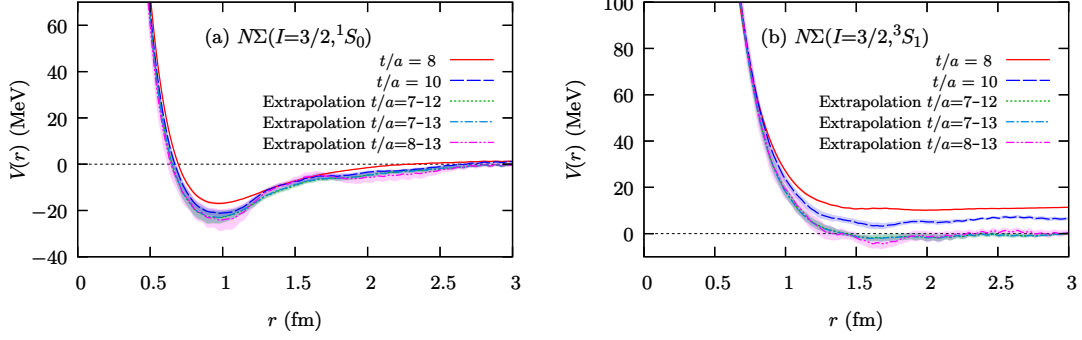


Figure 4: Extrapolated potentials of $N\Sigma(I = 3/2)$. The results with different fitting ranges are compared to the results with the local HAL QCD method.

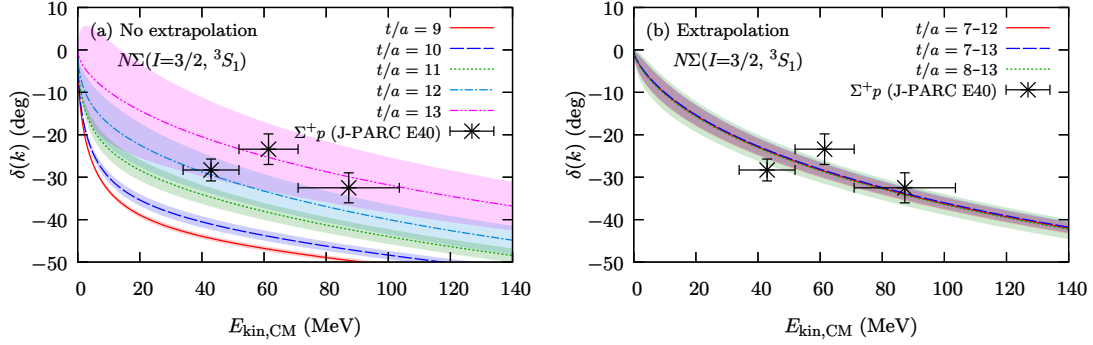


Figure 5: Phase shifts calculated with the analytic forms fitted to the extracted potential. Panel (a) shows the phase shifts for the potentials obtained from local time slices using the HAL QCD method. Panel (b) shows the phase shifts calculated from the extrapolated potentials with different fitting ranges of t/a . The two-range Gaussian plus the Yukawa potential for the one pion exchange is used for the analytic form fitted to the potentials. The experimental data shown by black dots are taken from Ref. [6] assuming a negative phase shift $\delta(k) < 0$.

exponential fitting, which shows that the assumption of the single exponential (9) is actually a very good assumption in the $\Xi\Xi$ channel. A similar method has been examined in Ref. [18] with b_c being determined based on the physical considerations.

It is non-trivial whether the single-exponential assumption works well also in the $N\Sigma(I = 3/2)$ channel. Figure 3 shows that the assumption is consistent also in the $N\Sigma(I = 3/2)$ channel. We only have about five meaningful time points, but both 1S_0 and 3S_1 are consistent with the single-exponential assumption (9). The small χ^2 value in 1S_0 is because χ^2 is calculated in the uncorrelated form, where the correlations between different times are ignored. The small value implies that the statistical error is dominated by the one with strong correlations among different times for 1S_0 .

We then determine the potential. We first determine the exponent b in Eq. (9) by fitting the exponential form (9) at $r \geq 3$ fm, assuming that the physical potential $V_{\text{el}}(r)$ is negligibly small at large r : $V_{\text{el}}(r > 3 \text{ fm}) = 0$. Then, we perform the linear fitting with the fixed b at each r . We obtain $V_{\text{el}}(r)$ as the extrapolated potential. Figure 4 shows the extracted potentials. The extrapolations

are performed with different time ranges. The extrapolated potentials vanish at large r as expected. While the potentials with the conventional HAL QCD method using local time slices has a large time dependence, the time dependence of the extrapolated potentials is sufficiently suppressed. The exclusion of the largest time slice $t/a = 13$, which has large statistical errors, does not affect the potential much (see the green dotted line). On the other hand, the exclusion of the smallest time slice $t/a = 7$ significantly increases the statistical errors, and the resulting potential also starts to oscillate.

The analytic forms of the potentials can be determined by fitting them to the obtained potentials. Then, they can be used to calculate quantities such as the phase shift, as shown in Fig. 5. In Fig. 5, we used the two-range Gaussian forms plus a Yukawa potential for the one pion exchange as the analytic form. Panel (a) shows the results with the potentials directly calculated from the conventional HAL QCD method, which is significantly affected by the constant offset caused by inelastic contamination. Panel (b) shows the results with the potentials extracted by the extrapolation, where we find that the dependence of the phase shift on the fitting t/a range is negligible.

We shall comment on the extracted decay rate b of the inelastic contamination in the exponent of Eq. 9. The extracted decay rate has been consistently around $b \simeq 0.3 = 700$ MeV in both $\Xi\Xi$ and $N\Sigma$, which is significantly larger than the expected gap of the first excited state. This is considered to be due to the cancellation happening with the prescription (4) of normalizing the four-point function by the two-point function.

5. Conclusion

We have investigated the strangeness $S = -1$ baryon–baryon potentials at the physical point using the time-dependent HAL QCD method on the gauge configurations HAL-conf-2023 [14]. The $S = -1$ sector of the potentials suffers from a poor signal-to-noise ratio. In particular, the Pauli-forbidden channels ($I = 1/2, {}^1S_0$) and ($I = 3/2, {}^3S_1$) receive severe contamination from inelastic excited states within the time-dependent HAL QCD method, which uses consecutive three time slices. We attempted to remove the inelastic contamination by extrapolating the extracted potentials to $t \rightarrow \infty$ by assuming the single-exponential form of the time dependence of the potential. While a strong time dependence of phase shift is observed with the original potentials, the phase shift for the extrapolated potentials has almost no dependence on the fitting time range. In the future, we should carefully check consistency and robustness of this extrapolation method, and apply the method to the full analysis of the $S = -1$ baryon–baryon interactions including the tensor force and the D wave.

Acknowledgment

We thank the members of the HAL QCD Collaboration for fruitful discussions. The generation of the gauge configurations and the measurements of the correlation functions are performed on the Fugaku supercomputer. This work has been supported by JSPS KAKENHI Grant Numbers JP19K03879, JP23H05439, JP23K13102, and JP25H01272.

References

- [1] P. Demorest, T. Pennucci, S. Ransom, M. Roberts and J. Hessels, *Nature* **467**, 1081-1083 (2010).
- [2] J. Antoniadis *et al.* *Science* **340**, 6131 (2013).
- [3] N. K. Glendenning and S. A. Moszkowski, *Phys. Rev. Lett.* **67**, 2414-2417 (1991).
- [4] A. Jinno, K. Murase, Y. Nara and A. Ohnishi, *Phys. Rev. C* **108**, no.6, 065803 (2023).
- [5] K. Miwa *et al.* [J-PARC E40], *Phys. Rev. C* **104**, no.4, 045204 (2021).
- [6] T. Nanamura *et al.* [J-PARC E40], *PTEP* **2022**, no.9, 093D01 (2022).
- [7] Y. Ichikawa *et al.* *EPJ Web Conf.* **271**, 02012 (2022).
- [8] Y. Nara, A. Jinno, K. Murase and A. Ohnishi, *Phys. Rev. C* **106**, no.4, 044902 (2022).
- [9] K. Morita, T. Furumoto and A. Ohnishi, *Phys. Rev. C* **91**, no.2, 024916 (2015).
- [10] L. Adamczyk *et al.* [STAR], *Phys. Rev. Lett.* **114** (2015) no.2, 022301.
- [11] S. Acharya *et al.* [ALICE], *Phys. Rev. C* **99** (2019) no.2, 024001.
- [12] N. Ishii, S. Aoki and T. Hatsuda, *Phys. Rev. Lett.* **99**, 022001 (2007).
- [13] N. Ishii *et al.* [HAL QCD], *Phys. Lett. B* **712**, 437-441 (2012).
- [14] T. Aoyama *et al.* [HAL QCD], *Phys. Rev. D* **110**, no.9, 094502 (2024).
- [15] H. Nemura [LATTICE-HALQCD], *AIP Conf. Proc.* **2130**, no.1, 040005 (2019).
- [16] H. Nemura, *PoS LATTICE2021*, 272 (2022).
- [17] T. Miyamoto *et al.*, *Phys. Rev. D* **101**, no.7, 074514 (2020).
- [18] J. Bulava *et al.* [Baryon Scattering], *Phys. Rev. C* **113**, no.2, 024002 (2026) doi:10.1103/d2hg-h6d4 [arXiv:2505.05547 [hep-lat]].